ADVANCED OPTICAL MATERIALS
www.advopticalmat.de

Circular Dichroism in Higher-Order Diffraction Beams from Chiral Quasiplanar Nanostructures

*Christian Kuppe, Calum Williams, Jie You, Joel T. Collins, Sergey N. Gordeev, Timothy D. Wilkinson, Nicolae-Coriolan Panoiu, and Ventsislav K. Valev**

Miniaturization down to the nanoscale has enabled a new paradigm of ultrathin optical devices, capable of manipulating the direction, polarization, and frequency of light. Great interest is drawn by the promising prospects of deep-subwavelength material dimensions. However, interesting properties and opportunities offered by structures with sizes comparable to the wavelength of light appear to have been overlooked. Here, quasiplanar chiral arrays made of gold are considered and show that higher-order diffracted beams can yield extremely large chiroptical responses for optical frequencies. The chosen sample geometry demonstrates spectrally tunable polarization conversion and extremely large circular dichroism. Experimental and numerical data are in good agreement, for both sample chiral forms, and for the complementary geometries under Babinet's principle. Specifically, the experimental results show that the fractional circular dichroism (CD) can be as high as 20%, in the third-order diffraction beam. Based on the numerical results, a great potential for improvement is anticipated, which makes higher-order diffraction CD a very promising candidate for ultrathin optical applications.

Due to their lack of mirror symmetry, chiral nanomaterials have enabled both fascinating physical properties, such as negative refractive index or superchiral light, and exciting technological applications.[1,2] The latter include next-generation optical components,[3,4] nanorobotics, and chiral molecular sensing.[5–10] Several relevant reviews have been published recently.[11–13]

Circular dichroism (CD) is routinely used to investigate chiral nanomaterials, which absorb and scatter left- and right-circularly polarized light (LCP and RCP) differently depending on the handedness of the nanostructures. Such nanostructures can give rise to much stronger CD than chiral molecules, in part because the pitch of the twist is better matched to optical wavelengths.[14–18] In metal nanoparticles, localized surface plasmon resonances (coherent oscillations of the free electrons at the surface) can greatly enhance the light–matter interaction and, by extension, the chiroptical interactions.[19–22] In general, chiroptical interactions can be enhanced by increasing the chirality parameter of the nanostructures[23,24] or of light (optical chirality).[25] Most investigations have been performed on structures with subwavelength dimensions, chiefly because this enables their theoretical treatment within an effective medium approximation.[26] However, diffractive chiral nanomaterials are also of great interest because the CD measured in the diffracted beams can be orders of magnitude larger than that in the zeroth-order beam.[27] Although previous studies have addressed the CD in diffracted beams, those studies were limited to zeroth- and first-order beams.[28–34]

Here, we investigate chiral metal nanostructures that exhibit large CD in the diffracted beams. We show that, for our structures, the third-order diffraction beam gives the strongest CD response. This CD changes sign depending on wavelength. Our results are validated by a good agreement between numerical and experimental data. Moreover, we establish the robustness of our findings by making use of Babinet's principle. In order to identify the origin of the effect, we provide numerical simulations of the near field. These simulations show that for LCP and RCP beams, a difference in the electromagnetic response at the surface can be linked to the far-field CD.

The samples measured in this study were fabricated using electron beam lithography (EBL)– a detailed description can be found in the Experimental Section. In **Figure 1**a, the dimensions and depth profile are schematically shown. The gold U-shaped structures are 1 μm in length, have a separation of 200 nm, and a highly subwavelength thickness. Each square unit cell consists of four U-shaped gold structures rotated by 90° with respect to each other. The dimensions of the actual

C. Kuppe, J. T. Collins, Dr. S. N. Gordeev, Dr. V. K. Valev
Centre for Photonics and Photonic Materials
and Centre for Nanoscience and Nanotechnology
University of Bath
Bath BA2 7AY, UK
E-mail: v.k.valev@bath.ac.uk
Dr. C. Williams, Prof. T. D. Wilkinson
Electrical Engineering Division
Department of Engineering
University of Cambridge
9 JJ Thomson Avenue, Cambridge CB3 0FA, UK
Dr. J. You, Prof. N.-C. Panoiu
Department of Electronic and Electrical Engineering
University College London
Torrington Place, London WC1E 7JE, UK
The ORCID identification number(s) for the author(s) of this article can be found under https://doi.org/10.1002/adom.201800098.

DOI: 10.1002/adom.201800098

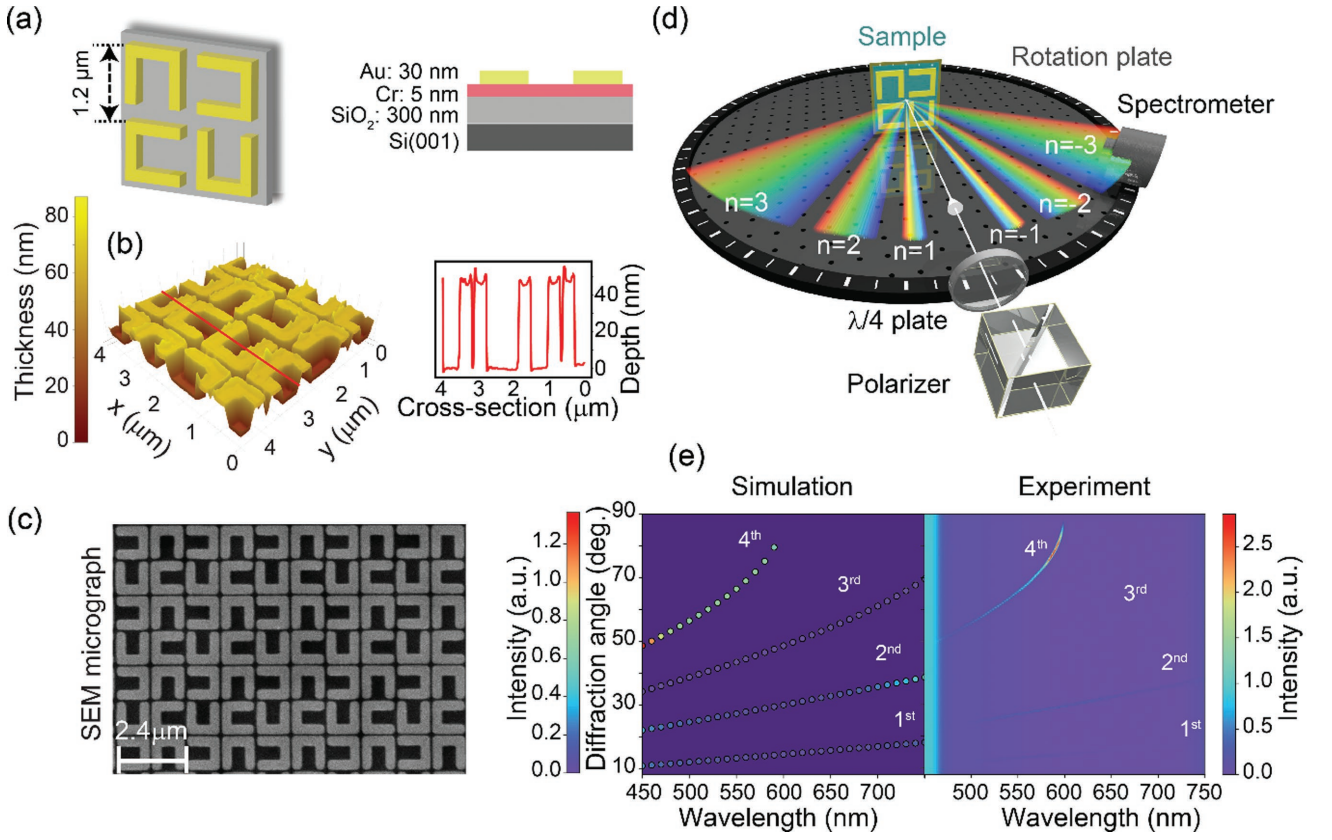

Figure 1. Panel (a) gives the schematic dimensions and depth of the U-shaped gold arrays and panel (b) shows the AFM image (left) and depth profile for the cross-section indicated by the red line across the AFM image. The SEM microscopic image of the array on a larger scale is shown in panel (c). In panel (d), the experimental setup of CD spectrometer is given. A supercontinuum fiber source with a range of 450–1050 nm is used. A quarter wave plate selectively provides LCP and RCP light. As the detection is limited to the visible region, a short-pass filter (<750 nm) is used. The sample is positioned orthogonally to the angle of incidence and the detector is located on a rotation stage measuring the in-plane diffraction orders. In panel (e), the resulting intensities for RCP light are shown both numerically and from experiment, which are in very good agreement showing the diffraction order beams n = 1–3 as weak and a significantly stronger fourth-order beam.

fabricated nanostructures were established using atomic force microscopy (AFM) (Figure 1b) and scanning electron microscopy (SEM) (Figure 1c). The experimental setup for higher-order diffraction CD spectrometry is illustrated in Figure 1d. Here, a supercontinuum fibre laser source was used to provide 450–750 nm illumination. The polarization state of the incident beam was controlled by a linear polarizer and a quarter wave plate. The sample was mounted normal to the plane of incidence and an optical fiber, leading to a spectrometer placed on a rotation stage, was centered on the sample. Within this setup design only the horizontal-plane diffraction beams were measured, as indicated in the figure. Our study encompassed up to four diffraction order beams (not including the zeroth-order beam), see Figure 1e. For our samples, the fourth-order diffraction beam had the strongest intensity, as demonstrated both numerically and experimentally. The spatial distribution of the diffraction order beams followed the grating equation for diffraction, that is, $d \sin\theta = n\lambda$, where d is the lattice parameter (equal to unit cell size 2.4 μm), θ represents the angle of diffraction, n is an integer number that defines the diffraction order, and λ is the wavelength.

Here, we define the normalized CD as the difference over sum ratio, that is, $\mathrm{CD} = (I_{\mathrm{LCP}} - I_{\mathrm{RCP}})/(I_{\mathrm{LCP}} + I_{\mathrm{RCP}})$, where I_{LCP} and I_{RCP} are the intensities measured for LCP and RCP, respectively.[35–38]

For consistency, we investigated both enantiomorphs, that is, U-shaped and mirrored U-shaped structures, both numerically and experimentally, see **Figure 2**a–d. Figure 2a shows a map of the numerical data, with the angle of each beam along the y-axis and the wavelength along the x-axis. The CD is visible as color-coded values (red–blue).[39] It is immediately obvious that the CD in the third-order diffracted beam dominates, with the first, second, and fourth orders exhibiting nearly no CD in comparison. Moreover, in the third order, a characteristic bisignate (i.e., of two signs) CD is clearly apparent. A similar bisignate CD is also displayed in the experimental maps (Figure 2b). The difference is that in the experimental maps, the zero-CD crossing of the bisignate effect is blueshifted. This difference can be attributed to fabrication imperfections, as compared to the idealized geometries in the numerical simulations.[40–43] Such imperfections can be seen in the AFM image and corresponding depth profile (Figure 1b). The imperfections are typically due to electron beam dosage during the EBL processes or could occur during the lift-off procedure, for instance because resist remains attached to the corners of nanostructures.

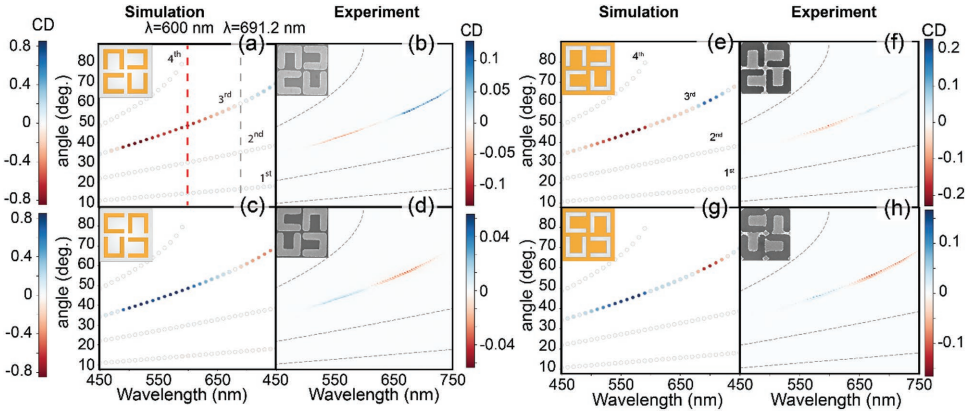

Figure 2. Comparison of experimental and numerical CD response for the third diffraction order beams for the U-shaped chiral arrays. Panels (a) and (b) show the numerical and experimental results for the U-shaped structures, respectively. The red dashed line in panel (a) represents the wavelength of maximum CD, while the gray dashed line marks the position of vanishing CD. In contrast, panels (c) and (d) show this effect for the opposite handedness. The insets show the schematic presentation used for the simulations and the SEMs for the experiments. The same analysis has been carried out for the complementary trenches, given in panels (e–h). The simulations clearly show that the third-order diffraction beam is the most dominant. Therefore, we only show the third-order diffraction beam in the experimental graph, while the gray dashed lines indicate the position of the other diffraction beams. Further, upon inversing the structures, the results show that CD is invariant and validates the applicability of Babinet's principle. Numerical and experimental data are in good agreement.

Upon simulating and measuring the mirrored U-shaped nanostructures, similar results of opposite sign are obtained. Figure 2c shows the numerical data for the mirrored U-shaped nanostructures, where the bisignate CD is opposite (i.e., blue–red transition). This trend is confirmed by the experimental results presented in Figure 2d.

Moreover, in order to firmly establish the robustness of our results, we made use of Babinet's principle.[44–47] Figure 2e–h presents numerical simulation data and experimental results from the complementary inverse U-shaped samples, that is, U-shaped trenches within a continuous gold film. The data from these complementary structures unambiguously match those from the U-shaped nanostructures; bearing in mind that those are two sets of samples, with respective intrinsic imperfections.

The maximum absolute values of the CD are as high as 80% for the simulations and 20% for the experiment. The difference in theoretical and measured yield can be explained with the aforementioned imperfections, intrinsic to the fabrication process, and measurement conditions. Moreover, the difference in CD for the solid structures and their complementary trenches is also attributable to the thickness of the nanostructures. Indeed, Babinet's principle is only strictly valid for infinitely thin, ideal surfaces. Previous studies have established that the principle holds for samples of small finite thickness.[48] Our results are therefore an extension of these studies for even thicker samples (more than double).

A direct comparison between Figure 2 and Figure 1e demonstrates a difference between absolute intensity and CD of the diffracted light, while the diffracted intensity for circularly polarized light is strongest in the fourth order, the CD is strongest in the third order. A large absolute intensity for LCP and RCP light does not necessarily lead to a large normalized CD, as it is clear from the formula, $CD = (I_{LCP} - I_{RCP})/(I_{LCP} + I_{RCP})$. Indeed, for a given absolute difference in intensity $\Delta I = I_{LCP} - I_{RCP}$, CD would be larger if I_{LCP} and I_{RCP} are small. Note also that in our numerical simulations the array is assumed to be infinite as periodic boundary conditions are used in the transverse directions, whereas the fabricated structures are finite in the transverse directions. This also contributes to the observed discrepancies between the computational predictions and experimental measurements. In order to understand the counterintuitive intensity distribution that is shown in Figure 1e, a comparison to a common diffraction grating consisting of a finite number, N, of identical and equally spaced line sources is instructive. For such optical diffraction gratings, the grating equation can be used to determine the spatial distribution of the intensity of the diffracted light

$$I = I_0 \frac{\sin^2\left(N\frac{\phi}{2}\right)}{\sin^2\left(\frac{\phi}{2}\right)}, \tag{1}$$

where I is the intensity, I_0 is the zeroth-order intensity, and ϕ is a phase defined by the angle made by the diffracted beam with respect to the plane of the diffraction grating.[49] For more complex gratings, the intensity of each diffracted beam is governed by the shape and nature of each unit cell. This complexity leads to the possibility of introducing additional design parameters that can be exploited to create a variety of power distributions in the diffracted beams, such as the duty cycle, defined as the ratio between the feature dimensions and the period of the grating.[50] This factor alone can cause extreme changes in the envelope function of the intensity distribution and has spurred interest in its design, recently.[51–54]

The grating equation assumes periodically distributed point sources interfering in the far field. In our experiments, the periodic near-field hotspots themselves are large compared to the wavelength of light. Because of this, they do not behave as point sources, and thus the far-field diffraction pattern depends on both the periods of the array and the nontrivial

angle-modulated far-field response of individual unit cells. Klimov et al.[55] recently proposed an intuitive method to cope with such structures theoretically. Specifically, the authors describe the far field of such nanostructures as

$$E_{\text{far-field}} = \sum_{n=-\infty}^{\infty} \sum_{m=-\infty}^{\infty} C_{nm} \exp\left(-ik_{x,n}x\right)\exp\left(-ik_{y,m}y\right)\exp\left(-ik_{z,nm}z\right) \quad (2)$$

where, $k_{x,n} = 2\pi n/W$, $k_{y,m} = 2\pi m/W$, and $k_{z,nm} = -\sqrt{k^2 - k_{x,n}^2 - k_{y,m}^2}$ are the components of the wavevector associated with the n,m diffraction order, k is the wave number, W is the period of the grating, and x, y, z are Cartesian coordinates for a coordinate system located at the center of the array with the z-axis pointing away from the structure. The Fourier coefficients C_{nm} can be calculated from the near field, that is

$$C_{nm} = \frac{1}{W^2}\int_0^W \int_0^W E_{\text{near-field}} \exp\left(i\left(k_{x,n}x + k_{y,m}y\right)\right)dx\,dy \quad (3)$$

These equations are general and, for simple gratings, they result in Equation (1). For all but the simplest cases, $E_{\text{near-field}}$ needs to be computed numerically.

The numerically computed far-field results shown in Figure 2 are a direct consequence of the near-field electric field distribution. Thus, to explore the origin of the chiroptical response measured, we used a rigorous Maxwell's equations solver in the frequency domain (detailed information can be found in the Experimental Section). The results for the U-shaped nanostructures are displayed in **Figure 3**. The figure shows the color-coded electric field intensity, at the surface of the nanostructures, upon illumination at 600 (Figure 3a) and 691.2 nm (Figure 3b). While the former corresponds to the maximum CD, the latter corresponds to the wavelength at which the CD vanishes. For both Figure 3a,b, the left and right panels show data for LCP and RCP illumination, respectively. We can immediately see that there is no single-point source that could be assumed to dominate in the far-field projection; however, we can investigate the periodic field profile. At 600 nm illumination, the heat maps show a clear change in the intensity pattern. This is most prominent in the central region of the unit cells, which have been magnified (top panels). The central region is also where chiral coupling occurs between the four achiral U-shaped nanostructures, whereas the near-field intensity pattern in Figure 3a is chiral, that in Figure 3b is not. This behavior translates directly into the far-field effects reported in Figure 2 when Equations (2) and (3) are applied.

Using numerical simulations, we identified the origin of the effects reported here. Our solution is in agreement with other studies,[17,35,54] both numerical and experimental, showing that chiral currents, and associated near-fields at the surface of both chiral and achiral structures play a major role in determining the chiroptical response of a metasurface.

In conclusion, we demonstrate CD in higher-order diffraction beams, enabling us to clearly differentiate between both enantiomorphs of quasiplanar, U-shaped

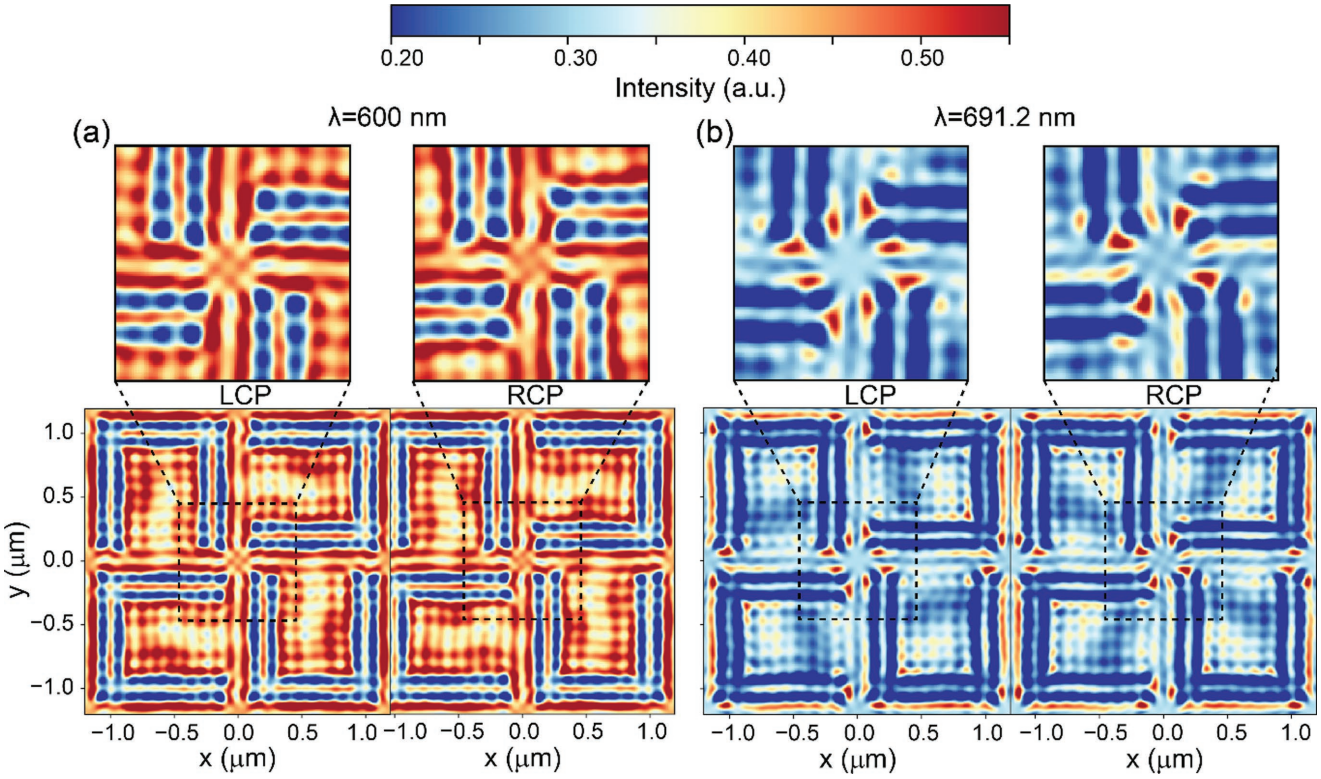

Figure 3. Near-field simulations at the surface of the samples illuminated with a) 600 nm giving maximum CD and b) 691.2 nm where the CD vanishes. The magnified central area is shown on top for each case, when illuminated with LCP (left) and RCP (right), respectively. We see a clear change in the normalized electric field intensity pattern in the central region, indicating that the source of the CD in the far-field originates from near-field sources. In particular, the optical near-field is strongly chiral in the case of maximum CD, whereas in the case when CD vanishes the profile of the optical near-field does not exhibit chirality.

nanostructures. Whereas previous studies limited themselves to the zeroth- or first-order diffraction,[28–34] we show that, for our samples, the third-order diffraction beam is the most dominant with respect to its chiroptical response. The CD was found to follow Babinet's principle. In addition, we identify chiral surface electric fields as the origin of the far-field chiroptical response. The chosen geometry allows a high degree of control over the polarization conversion and spatial properties of light and it is spectrally tuneable. Further control will be allowed through manipulating the diffraction form factor of such systems. This can be achieved specifically by adjusting the lattice parameters, unit geometry, and refractive indices of the metasurfaces. Our study calls for future research focusing on the nature of near-field sources and how they can be designed to control the far-field response in diffraction experiments. It can also be envisioned that diffracted beams could be used for enhanced CD spectroscopy of molecules as well as other devices used for optical sensing.

Experimental Section

Sample Fabrication: 10 mm x 10 mm x 525 µm single side polished Si(p-doped)-SiO_2(300 nm) samples were sonicated in successive baths of acetone and isopropyl alcohol (IPA) for 10 min, blow dried with compressed N_2 and dehydrated on a hotplate (200 °C, 20 min). Polymethyl-methacrylate (PMMA) A4 950 k positive-tone photoresist was spin coated (5000 rpm, 45 s) and baked (180 °C, 2 min), resulting in a final thickness of ≈150 nm. 80 kV electron beam lithography (Nanobeam, nB-1) was used for the high-resolution patterning, with exposure conditions: area dose ≈10 cm^{-2}, operating current 5 nA s^{-1}, and main-field/subfield apertures of 50/6 µm. Resist development was carried out in a 1:3 solution of methyl-isobutyl-ketone): IPA for 10 s. Deposition of Cr/Au (5/30 nm) was performed using a thermal evaporator at a base pressure ≈1 × 10^{-6} mbar, at an evaporation rate ≈0.1 nm s^{-1}. Resist lift-off was carried out in *N*-methyl-2-pyrrolidone (NMP) at an elevated temperature of 60 °C for 4 h, followed by fresh NMP sonication, acetone, and IPA rinse. For nanoscale surface quality inspection, a Carl Zeiss scanning electron microscope operating at 3 keV was used.

Sample Characterization: AFM experiments were carried out using a Multimode Scanning Probe Microscope (Veeco, Plainview, NY) with a Nanoscope IIIA controller. Images were obtained in contact mode under ambient conditions. A Pointprobe-Plus Silicon-SPM-Sensor AFM probe (PPP, Nanosensors, Neuchâtel, Switzerland) with a force constant of 0.039 N m^{-1} was used for imaging.

The additional SEM shown in Figure 1c was taken with the JEOL SEM6480LV operating in the backscattering mode at 10 keV.

Experimental Setup: The experimental setup consisted of a Fianium SC400-2 2 W laser source with a 1064 nm output wavelength and 20 MHz repetition rate and a 5 ps pulse spliced to an in-house fabricated supercontinuum fiber, described in ref. [56], providing a spectrum between 450 and 1050 nm. A short-pass filter was used to only allow light in the spectral region between 450 and 750 nm. Two linear Glan-Laser polarizers were used to control the power output and a remotely controlled quarter wave plate to selectively produce LCP and RCP light. The sample was mounted on an alignment disk, which in turn was mounted on an in-house designed adapter placed in the center of an optical breadboard. The breadboard was mounted on a remotely controlled rotation stage. The diffracted light from the sample was collected via a 400 µm diameter multimode fiber mounted on the edge of the breadboard at a distance of 25 cm and measured with an Ocean Optics QE Pro spectrometer. The automated setup used a step size of 0.5° and the spectrometer used an integration time of 250 ms and was averaged over eight scans.

Simulations: The optical near-field and the intensity of the diffracted beams were computed numerically using the rigorous coupled wave analysis method, implemented in Synopsys RSoft DiffractMOD, a commercially available software. In this method, both the distribution of the dielectric constant and electromagnetic field were decomposed in Fourier series, the corresponding Fourier coefficients being computed using the boundary conditions at the top and bottom of the structure. These coefficients were subsequently used to calculate the optical near field and the intensities of the diffracted beams. The frequency dispersion of the permittivity of Au, Cr, and SiO_2 was fully incorporated in the simulations. Moreover, $N = 20$ harmonics was used for each transverse dimension, which amounted to a total of $(2N + 1)^2 = 1681$ harmonics.

Acknowledgements

V.K.V. acknowledges support from the Royal Society through the University Research Fellowships. J.Y. acknowledges support from the China Scholarship Council (CSC). N.C.P. acknowledges support from the European Research Council (ERC) (ERC-2014-CoG-648328). C.W. and T.D.W. acknowledge support from the Engineering and Physical Sciences Research Council (EPSRC) and the Integrated Photonics and Electronic Systems Centre for Doctoral Training (Grant number: EP/L015455/1). The authors are grateful to Dr. W. Wadsworth for providing the Fianium laser source and to Dr. J.M. Stone for the supercontinuum fiber. In addition, the authors thank Dr. S. Yerolatsitis for the support with respect to fiber handling. The authors thank Prof. S. P. Collins from the Diamond Institute for his feedback. All data used for this paper are openly available from the University of Bath data archive at https://doi.org/10.15125/BATH-00479.

Conflict of Interest

The authors declare no conflict of interest.

Keywords

Babinet's principle, chirality, circular dichroism, diffraction, nanophotonics

Received: January 24, 2018
Published online:

[1] J. B. B. Pendry, *Science* **2004**, *306*, 1353.
[2] Y. Tang, A. E. Cohen, *Phys. Rev. Lett.* **2010**, *104*, 1.
[3] V. K. Valev, A. V. Silhanek, B. De Clercq, W. Gillijns, Y. Jeyaram, X. Zheng, V. Volskiy, O. A. Aktsipetrov, G. A. E. Vandenbosch, M. Ameloot, V. V. Moshchalkov, T. Verbiest, *Small* **2011**, *7*, 2573.
[4] Y. Shen, D. Ye, I. Celanovic, S. G. Johnson, J. D. Joannopoulos, M. Soljačić, *Science* **2014**, *343*, 1499.
[5] A. M. Maier, C. Weig, P. Oswald, E. Frey, P. Fischer, T. Liedl, *Nano Lett.* **2016**, *16*, 906.
[6] D. Schamel, A. G. Mark, J. G. Gibbs, C. Miksch, K. I. Morozov, A. M. Leshansky, P. Fischer, *ACS Nano* **2014**, *8*, 8794.
[7] T. C. Lee, M. Alarcón-Correa, C. Miksch, K. Hahn, J. G. Gibbs, P. Fischer, *Nano Lett.* **2014**, *14*, 2407.
[8] E. Hendry, T. Carpy, J. Johnston, M. Popland, R. V. Mikhaylovskiy, A. J. Lapthorn, S. M. Kelly, L. D. Barron, N. Gadegaard, M. Kadodwala, *Nat. Nanotechnol.* **2010**, *5*, 783.
[9] E. Hendry, R. V. Mikhaylovskiy, L. D. Barron, M. Kadodwala, T. J. Davis, *Nano Lett.* **2012**, *12*, 3640.
[10] B. Liu, C. Song, D. Zhu, X. Wang, M. Zhao, Y. Yang, Y. Zhang, S. Su, J. Shi, J. Chao, H. Liu, Y. Zhao, C. Fan, L. Wang, *Small* **2017**, *13*, 1603991.
[11] J. T. Collins, C. Kuppe, D. C. Hooper, C. Sibilia, M. Centini, V. K. Valev, *Adv. Opt. Mater.* **2017**, *5*, 1700182.

[12] X. Wang, Z. Tang, *Small* **2017**, *13*, 1601115.
[13] L. Wu, W. Zhang, D. Zhang, *Small* **2015**, *11*, 5004.
[14] M. Caricato, A. K. Sharma, C. Coluccini, D. Pasini, *Nanoscale* **2014**, *6*, 7165.
[15] C. Chang, X. Wang, Y. Bai, H. Liu, *TrAC, Trends Anal. Chem.* **2012**, *39*, 195.
[16] M. C. Dos Santos, O. Kesler, A. L. M. Reddy, *J. Nanomater.* **2012**, *2012*, 3127.
[17] A. O. Govorov, Z. Fan, P. Hernandez, J. M. Slocik, R. R. Naik, *Nano Lett.* **2010**, *10*, 1374.
[18] M. Retsch, M. Tamm, N. Bocchio, N. Horn, R. Förch, U. Jonas, M. Kreiter, *Small* **2009**, *5*, 2105.
[19] V. K. Valev, J. J. Baumberg, C. Sibilia, T. Verbiest, *Adv. Mater.* **2013**, *25*, 2517.
[20] S. A. Maier, M. L. Brongersma, P. G. Kik, S. Meltzer, A. A. G. Requicha, H. A. Atwater, *Adv. Mater.* **2001**, *13*, 1501.
[21] J. Liu, L. Yang, Z. Huang, *Small* **2016**, *12*, 5902.
[22] C. Hao, L. Xu, W. Ma, L. Wang, H. Kuang, C. Xu, *Small* **2014**, *10*, 1805.
[23] S. S. Oh, O. Hess, *Nano Convergence* **2015**, *2*, 1.
[24] Y. Zhao, L. Xu, W. Ma, L. Liu, L. Wang, H. Kuang, C. Xu, *Small* **2014**, *10*, 4770.
[25] Y. Tang, A. E. Cohen, *Science* **2011**, *332*, 333.
[26] O. Kidwai, S. V. Zhukovsky, J. E. Sipe, *Phys. Rev. A* **2012**, *85*, 53842.
[27] V. K. Valev, J. J. Baumberg, B. De Clercq, N. Braz, X. Zheng, E. J. Osley, S. Vandendriessche, M. Hojeij, C. Blejean, J. Mertens, C. G. Biris, V. Volskiy, M. Ameloot, Y. Ekinci, G. A. E. Vandenbosch, P. A. Warburton, V. V Moshchalkov, N. C. Panoiu, T. Verbiest, *Adv. Mater.* **2014**, *26*, 4074.
[28] A. Potts, W. Zhang, D. M. Bagnall, *Appl. Phys. B* **2010**, *99*, 679.
[29] P. Pagliusi, C. Provenzano, A. Mazzulla, L. Giorgini, G. Cipparrone, *Appl. Spectrosc.* **2008**, *62*, 465.
[30] Y. Tanaka, S. P. Collins, S. W. Lovesey, M. Matsumami, T. Moriwaki, S. Shin, *J. Phys.: Condens. Matter* **2010**, *22*, 122201.
[31] V. K. Valev, N. Smisdom, A. V. Silhanek, B. De Clercq, W. Gillijns, M. Ameloot, V. V. Moshchalkov, T. Verbiest, *Nano Lett.* **2009**, *9*, 3945.
[32] B. Bai, Y. Svirko, J. Turunen, T. Vallius, *Phys. Rev. A: At. Mol. Opt. Phys.* **2007**, *76*, 023811.
[33] T. Roy, A. E. Nikolaenko, E. T. F. Rogers, *J. Opt.* **2013**, *15*, 85101.
[34] A. Potts, W. Zhang, D. M. Bagnall, *Phys. Rev. A* **2008**, *77*, 43816.
[35] B. Frank, X. Yin, M. Schäferling, J. Zhao, S. M. Hein, P. V. Braun, H. Giessen, *ACS Nano* **2013**, *7*, 6321.
[36] M. Decker, R. Zhao, C. M. M. Soukoulis, S. Linden, M. Wegener, *Opt. Lett.* **2010**, *35*, 1593.
[37] F. Fang, Y. Cheng, H. Liao, *Optik* **2014**, *125*, 6067.
[38] J. Kaschke, L. Blume, L. Wu, M. Thiel, K. Bade, Z. Yang, M. Wegener, *Adv. Opt. Mater.* **2015**, *3*, 1411.
[39] R. Kuroda, T. Harada, *Comprehensive Chiroptical Spectroscopy: Instrumentation, Methodologies, and Theoretical Simulations*, Vol. *1*, John Wiley & Sons, Inc. Hoboken, New Jersey **2012**, p. 91.
[40] Z. Fan, A. O. Govorov, *J. Phys. Chem. C* **2011**, *115*, 13254.
[41] W. Zhang, A. Potts, D. M. Bagnall, *J. Opt. A: Pure Appl. Opt.* **2006**, *8*, 878.
[42] K. Hannam, D. A. Powell, I. V. Shadrivov, Y. S. Kivshar, *Phys. Rev. B* **2014**, *89*, 1.
[43] S.-C. Jiang, X. Xiong, Y.-S. Hu, S.-W. Jiang, Y.-H. Hu, D.-H. Xu, R.-W. Peng, M. Wang, *Phys. Rev. B* **2015**, *91*, 125421.
[44] K. Hannam, D. A. Powell, I. V. Shadrivov, Y. S. Kivshar, *Appl. Phys. Lett.* **2013**, *102*, 201121.
[45] Z. Li, K. B. Alici, E. Colak, E. Ozbay, *Appl. Phys. Lett.* **2011**, *98*, 161907.
[46] W. Gao, W. Y. Tam, *J. Opt.* **2011**, *13*, 15101.
[47] M. Hentschel, T. Weiss, S. Bagheri, H. Giessen, *Nano Lett.* **2013**, *13*, 4428.
[48] T. Zentgraf, T. P. Meyrath, A. Seidel, S. Kaiser, H. Giessen, C. Rockstuhl, F. Lederer, *Phys. Rev. B* **2007**, *76*, 33407.
[49] R. Feynman, R. Leighton, M. Sands, *The Feynman Lectures on Physics, Vol.1: The New Millennium Edition: Mainly Mechanics, Radiation, and Heat (1964)*, Basic Books, New York, NY, USA **2011**, p. 30.
[50] D. C. O'Shea, T. J. Suleski, A. D. Kathman, D.W Prather, *Diffractive Optics – Design, Fabrication, and Test*, SPIE, Bellingham, WA, USA **2003**, p. 83.
[51] L. Liu, X. Zhang, M. Kenney, X. Su, N. Xu, C. Ouyang, Y. Shi, J. Han, W. Zhang, S. Zhang, *Adv. Mater.* **2014**, *26*, 5031.
[52] A. Pors, O. Albrektsen, I. P. Radko, S. I. Bozhevolnyi, *Sci. Rep.* **2013**, *3*, 2155.
[53] D. Lin, P. Fan, E. Hasman, M. L. Brongersma, *Science* **2014**, *345*, 298.
[54] M. Hentschel, M. Schäferling, T. Weiss, N. Liu, H. Giessen, *Nano Lett.* **2012**, *12*, 2542.
[55] V. V. Klimov, I. V. Zabkov, A. A. Pavlov, R.-C. Shiu, H.-C. Chan, G. Y. Guo, *Opt. Express* **2016**, *24*, 6172.
[56] J. M. Stone, J. C. Knight, *Opt. Express* **2008**, *16*, 2670.